International Journal of Bifurcation and Chaos, Vol. 11, No. 11 (2001) 2823–2836

WAVE MIXING IN A BULK PHOTOREFRACTIVE MEDIUM: SPATIOTEMPORAL STRUCTURES AND AMPLITUDE EQUATIONS

O. SANDFUCHS and F. KAISER
Institute of Applied Physics, Darmstadt University of Technology, Hochschulstr. 4a, 64289 Darmstadt, Germany

M. R. BELIĆ
Institute of Physics, P.O. Box 57, 11001 Belgrade, Yugoslavia

Received October 3, 2000; Revised December 20, 2000

The counterpropagation of two laser beams through wave mixing in nonlinear optics may lead to spatiotemporal structures in the transverse beam profiles. We theoretically investigate the self-organization process of structures that arise in a photorefractive wave-mixing configuration with an external feedback mirror. The characteristic features mediated through the wave interaction in a bulk medium are discussed. Our group developed a beam propagation method that enabled us to perform numerical simulations beyond the first instability threshold. Primary and secondary spatiotemporal patterns, caused by the sluggish temporal response of the crystal in building reflection gratings, are observed. Analytically a Ginzburg–Landau equation for the order parameter and the corresponding longitudinal eigenfunctions of transverse modes, governing the propagation of the structures through the crystal, are derived and compared with our numerical results in one transverse dimension. First results of hexagonal patterns in two transverse dimensions are also presented.

1. Introduction

Ever since the initial experimental observations of hexagonal patterns [Honda, 1993; 1995; Banerjee *et al.*, 1995] due to counterpropagation of two optical beams in photorefractive (PR) crystals, pattern formation through PR two-wave mixing has become a growing field of nonlinear optics [Odoulov *et al.*, 1999]. In particular, the formation of patterns in a PR crystal with an external feedback mirror has been the topic of a number of recent articles. Structures, such as stripes and squares, have also been identified [Schwab *et al.*, 1998; Denz *et al.*, 1998], and very recently experiments on the competition of dynamical patterns [Denz *et al.*, 1998; Mamaev & Saffman, 1997] have been reported. Early experiments were accompanied by theoretical analyses of transverse modulational instabilities [Saffman *et al.*, 1994; Chernykh *et al.*, 1997; Honda & Banerjee, 1996]. However, there are only a few theoretical investigations beyond linear instability. In a paper by Lushnikov [1998] the stabilization of hexagonal mode structures using an amplitude equation formalism is explained.

In general, the cooperative effect of diffraction and nonlinear beam coupling leads to the formation of transverse patterns. The optical beams become spontaneously unstable against transverse modulations that start growing due to an absolute instability out of the initially smooth beam and grating profiles. The two-wave mixing between forward and backward propagating optical beams induces a refractive index grating which in turn couples the beams by Bragg diffraction [Yeh, 1993]. Bragg rather than Raman–Nath diffraction is present

because of the finite longitudinal extent of the crystal, i.e. a volume index grating is formed whose grating period is much shorter than the medium length. Two-wave mixing, in principle, involves co- or counterpropagating pump beams forming a transmission or reflection grating, respectively. The orientation of the crystal (i.e. one of the crystal's main axes, in solid state physics typically referred to as the c-axis) determines which of the gratings is dominant and provides the strongest coupling.

The model for the PR grating response originates from a charge transport model formulated by Kukhtarev *et al.* [1979]. Rigorous solutions of Kukhtarev's nonlinear material equations are computationally expensive [Singh *et al.*, 1997]. In the context of pattern formation through the interaction of counterpropagating waves via reflection gratings, it is particularly desirable to have an approximation of the grating response which is as simple as possible, but still good enough to account for the most phenomena observed. Otherwise, this problem quickly becomes unwieldy and renders analytical and even numerical treatments extremely difficult, even in the limit of one transverse dimension (1D).

The model of wave mixing introduced below is capable of elucidating the temporal evolution of the medium response, and has proven useful in the application to the spatiotemporal pattern formation through two-wave mixing and four-wave mixing in PR media [Krolikowski *et al.*, 1990; Belić *et al.*, 1995; Leonardy *et al.*, 1996; Sandfuchs *et al.*, 1998, 1999].

The setup for observation of transverse patterns in two-wave mixing with reflection gratings and one feedback mirror is presented in Fig. 1. The wave-mixing process is described by the slowly-varying envelope paraxial equations for the two beams [Krolikowski *et al.*, 1990; Yeh, 1993]

$$\partial_z A_1 + if\nabla_\perp^2 A_1 = -QA_2\,, \tag{1a}$$

$$-\partial_z A_2 + if\nabla_\perp^2 A_2 = Q^* A_1\,, \tag{1b}$$

where z is the propagation coordinate, scaled by the crystal length L, $f = L/(2k_0 w_0^2)$ is a measure of the magnitude of diffraction and is proportional to the inverse of the Fresnel number $F = (4\pi f)^{-1}$. k_0 denotes the wave number in the longitudinal direction within the crystal, and $\nabla_\perp^2$ is the transverse Laplacian, scaled by the beam waist w_0. Absorption losses have been neglected. Q is the amplitude of the reflection grating, whose temporal evolution

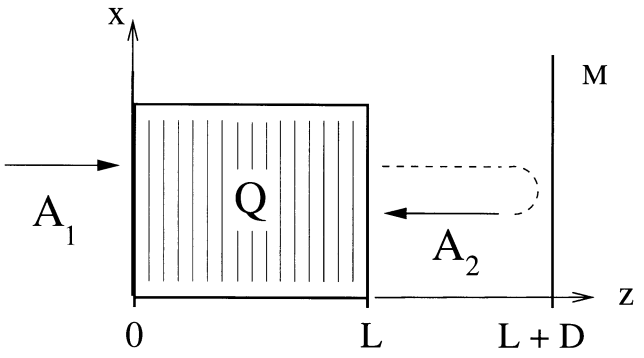

Fig. 1. Two-wave mixing configuration in reflection geometry, with a feedback mirror M. A_1 is the pump and A_2 is the reflected beam, Q is the grating amplitude. z indicates the direction of propagation and x represents the transverse plane.

is described by a relaxation equation of the form [Kukhtarev *et al.*, 1979]

$$\tau\partial_t Q + Q = \Gamma\,\frac{A_1 A_2^*}{|A_1|^2 + |A_2|^2}\,, \tag{2}$$

where τ is the relaxation time of the crystal, and Γ is the wave coupling constant. The assumption is that the dynamics of envelopes is slaved to the grating amplitude, because of its slow evolution, and that the spatial distribution of Q is determined by the spatial distribution of the beam envelopes.

The paper is organized as follows: the main part of the manuscript is devoted to pattern formation in one transverse dimension. Our investigation proceeds along two tracks, analytical and numerical. In Sec. 2 we derive a Ginzburg–Landau equation using a multiple scale expansion and define the pattern amplitudes and the corresponding longitudinal eigenfunctions. Section 3 presents numerical simulations of the full nonlinear model equations and the comparison to the analytical results. We discuss the basic features of the structure formation in order to understand the self-organization process in this photorefractive wave-mixing system. In Sec. 4 first numerical results of hexagonal patterns are presented that spontaneously form in two transverse dimensions (2D).

2. Multiple Scale Analysis

The self-organization process of patterns in the system presented here takes place in a bulk medium. The notion bulk medium refers to two conditions: first, patterns arise with the symmetry being imposed by the bulk parameters of the medium with-

out (or with negligible) influence by the boundaries, i.e. the lateral geometry of the system is of minor importance. The transition from boundary- to bulk-controlled patterns has been thoroughly discussed by Arecchi *et al.* [1993] for a PR optical oscillator. Second, for the interaction in a crystal, bulk medium emphasizes the fact that patterns are formed within a medium of *finite* longitudinal extent. As we have mentioned above, a volume index grating is built and within the crystal diffraction and PR nonlinear interaction take place simultaneously and are not locally separable. Outside the crystal free space propagation and the feedback mirror lead to a different transverse wave number selection depending on the mirror distance via the fractional Talbot effect [Tamburrini *et al.*, 1994].

The modulated structures are formed in the transverse plane and are observed at the output faces of the crystal. To understand their formation and propagation within the medium due to the interaction with the spatially modulated refractive index and the cooperative effects of the transverse modes, we perform a linear stability and a nonlinear amplitude analysis of Eqs. (1) and (2), by considering the time and space evolution of deviations from the fixed-point plane-wave solutions

$$A_{1;2}(x,\,z,\,t) = A^0_{1;2}(z)[1 + a_{1;2}(x,\,z,\,t)]\,, \quad \text{(3a)}$$

$$Q(x,\,z,\,t) = Q^0(z)[1 + q(x,\,z,\,t)]\,, \quad \text{(3b)}$$

where x is the transverse position vector scaled to the beam waist w_0. Upon substituting in Eqs. (1) and (2), one obtains an equivalent set of nonlinear wave-mixing equations

$$\partial_z a_1 + if\nabla^2_\perp a_1 = \Gamma\,\frac{1}{1+r}\,(a_1 - a_2 - q - a_2 q)\,, \quad \text{(4a)}$$

$$-\partial_z a_2 + if\nabla^2_\perp a_2 = \Gamma\,\frac{r}{1+r}\,(a_1 - a_2 + q^* + a_1 q^*)\,, \quad \text{(4b)}$$

$$\tau\partial_t q + q = \frac{(a_1 - a_2)(1+a_2^*) - r(a_1^* - a_2^*)(1+a_1)}{r(1+a_1)(1+a_1^*) + (1+a_2)(1+a_2^*)}\,, \quad \text{(4c)}$$

where the z-dependent ratio of fixed-point intensities is given by $r = |A^0_1(z)|^2/|A^0_2(z)|^2$. Equations (4a)–(4c) are supplemented with the boundary conditions

$$a_1(x,\,0,\,t) \equiv 0 \quad \text{(5a)}$$

$$a_2(x,\,L,\,t) = (FT)^{-1}[\exp(i\phi)FT[a_1(x,\,L,\,t)]]\,. \quad \text{(5b)}$$

The quantity $\phi = 2fK^2D/(n_0L)$ is the propagation phase with D being the distance to the feedback mirror, and K are the spatial Fourier modes (FT denotes Fourier transform), and n_0 is the crystal's homogeneous refractive index.

For the general procedure of multiple scale analysis in a bulk medium (where we follow an idea of Geddes *et al.* [1994]) it is convenient to choose a real basis for the state vectors of deviations via the following transformation (see Appendix A): $(a_1,\,a_1^*,\,a_2,\,a_2^*)^T \rightarrow \mathbf{U} = (U_1,\,U_2,\,U_3,\,U_4)^T$ and $(q,\,q^*)^T \rightarrow \mathbf{P} = (P_1,\,P_2)^T$ which brings Eqs. (4a)–(4c) into the general form

$$\mathcal{L}_{z,x}\mathbf{U} + \mathcal{M}_0\mathbf{P} = \boldsymbol{\mathcal{M}}_1(\mathbf{P}|\mathbf{U})\,, \quad \text{(6a)}$$

$$\mathcal{D}_t\mathbf{P} - \mathcal{N}_0\mathbf{U} = \boldsymbol{\mathcal{N}}_1(\mathbf{U}|\mathbf{U}) + \boldsymbol{\mathcal{N}}_2(\mathbf{U}|\mathbf{U}|\mathbf{U}) + \cdots \quad \text{(6b)}$$

Here the matrices $\mathcal{L}_{z,x}$ and $\mathcal{D}_t$ are the spatial and temporal derivative operators, respectively, and $\mathcal{M}_0$ and $\mathcal{N}_0$ are composed of the coefficients of the linear coupling between field and grating, and $\boldsymbol{\mathcal{M}}_i$ and $\boldsymbol{\mathcal{N}}_i$ are the vectors describing nonlinear field–grating and field–field interactions (for more details, see Appendix A).

To study analytically the formation of a one-dimensional pattern, we now perform a multiple scale analysis. It is based on the fact that in the neighborhood of a bifurcation point the temporal and spatial evolutions are separable into fast and slow scales. The PR coupling strength Γ is the bifurcation parameter, and the expansion parameter ε scales the distance from the critical point Γ_c at which the modulational instability starts growing. Expanding the bifurcation parameter, the temporal and spatial variables, and the field and grating amplitudes in terms of ε yields

$$\Gamma = \Gamma_c + \varepsilon\Gamma^{(1)} + \varepsilon^2\Gamma^{(2)} + \cdots \quad \text{(7a)}$$

$$t = T_0 + \varepsilon T_1 + \varepsilon^2 T_2 + \cdots \quad \text{(7b)}$$

$$x = X_0 + \varepsilon^\nu X_1 + \varepsilon^{2\nu} X_2 + \cdots \quad \text{(7c)}$$

$$\mathbf{U} = \mathbf{U}^{(0)} + \varepsilon^\nu\mathbf{U}^{(1)} + \varepsilon^{2\nu}\mathbf{U}^{(2)} + \cdots \quad \text{(7d)}$$

$$\mathbf{P} = \mathbf{P}^{(0)} + \varepsilon^\nu\mathbf{P}^{(1)} + \varepsilon^{2\nu}\mathbf{P}^{(2)} + \cdots \quad \text{(7e)}$$

Although, for simplicity, one usually chooses the scaling exponent such that $\nu = 1/2$, therefore *a priori* assuming a specific scaling behavior, we have taken $\nu = 1$, which leads to the same amplitude equation and, in addition, provides the correct

scaling behavior corresponding to the characteristics of the underlying bifurcation.

Collecting all terms linear in ε yields the linear instability threshold, the corresponding solution ansatz introduces the order parameter. Higher orders in ε describe the nonlinear interaction of spatial modes and result in the amplitude equation for the order parameter (Sec. 2.2).

2.1. *Linear instability and order parameter*

In the first order of ε one recovers the linear problem

$$\mathcal{L}^c_{z,X_0}\mathbf{U}^{(1)} + \mathcal{M}_0\mathbf{P}^{(1)} = 0\,, \tag{8a}$$

$$\mathcal{D}_{T_0}\mathbf{P}^{(1)} - \mathcal{N}_0\mathbf{U}^{(1)} = 0\,. \tag{8b}$$

At this point we outline the results from linear stability analyses [Saffman *et al.*, 1994; Honda & Banerjee, 1996; Sandfuchs *et al.*, 1998]. The deviations can be considered here as small perturbations, and they are expanded in the transverse Fourier ($X_0 = x \to K$) and in the temporal Laplace ($T_0 = t \to \lambda$) space, yielding an algebraic expression for $\mathbf{P}^{(1)}$. The linearized equations are cast into a matrix form

$$\begin{aligned}[\mathcal{L}_z(K) + \mathcal{M}_0\mathcal{D}(\lambda)^{-1}\mathcal{N}_0]\mathbf{U}^{(1)} \\ \equiv [\partial_z - \mathcal{A}(z;\,\lambda,\,K)]\mathbf{U}^{(1)} \\ = 0\end{aligned} \tag{9}$$

where the stability matrix reads as [Sandfuchs *et al.*, 1998]

$$\mathcal{A} = \begin{pmatrix} m_0^2\Gamma + (1-m_0^2)g(\lambda) & -fK^2 & 0 & 0 \\ fK^2 & 0 & 0 & s\sqrt{1-m_0^2}\,g(\lambda) \\ s\sqrt{1-m_0^2}\,g(\lambda) & 0 & 0 & -fK^2 \\ 0 & 0 & fK^2 & g(\lambda) \end{pmatrix}. \tag{10}$$

The temporal variations in Q that are due to the sluggish PR response result in the function $g(\lambda) = \Gamma\lambda\tau/(\lambda\tau+1)$.

In this particular basis the physics involved in the linear stability analysis becomes more obvious. The steady-state fixed-point solution contributes only through its modulation depth $m_0(z) = 2\sqrt{r}/(1+r)$ and a factor $s = \mathrm{sign}(1-r)$ to stability.

Owing to energy exchange of PR wave mixing Eq. (9) is nonautonomous and can only be solved analytically under the special constraint $R = 1$, which implies that $r = 1$ and $m_0 = 1$ so that the stability matrix is constant in z. The formal solution is then given by a linear flow matrix $\mathcal{F}(z) = \exp(\mathcal{A}z)$. Taking into account the mirror boundary condition we invert $\mathcal{F}(L)$ into a scattering matrix $\mathcal{S}_F(K)$. The poles of this matrix determine the properties of an absolute instability and lead to the threshold condition

$$\begin{aligned} 0 &= \det\,\mathcal{S}_F^{-1}(K) \\ &= \cos(\chi_1)\,\cos(\chi_2) + \left[\frac{\Gamma}{2}\cos(\phi)\,\cos(\chi_2) + fK^2\left(fK^2 - \frac{\Gamma}{2}\sin(\phi)\right)\mathrm{sinc}(\chi_2)\right]\mathrm{sinc}(\chi_1) \\ &\quad + \frac{g}{2}\left[\cos(\phi)\,\cos(\chi_1) + \left(\frac{\Gamma}{2} - fK^2\sin(\phi)\right)\mathrm{sinc}(\chi_1)\right]\mathrm{sinc}(\chi_2)\,, \end{aligned} \tag{11}$$

where $\chi_1^2 = (fK^2)^2 - \Gamma^2/4$ and $\chi_2^2(\lambda) = (fK^2)^2 - g^2/4$. Equation (11) reduces to Eq. (5) in [Honda & Banerjee, 1996] in the case of a stationary instability ($\lambda_c \equiv 0$). The threshold curve for the case $D = 0$ is displayed in Fig. 2. The uniform plane-wave solution for the beams loses stability through a saddle-node bifurcation at the threshold coupling constant $\Gamma_c L \approx 3.819$ with the critical transverse wave number $fK_c^2 \approx 2.592$. So above threshold ($\Gamma > \Gamma_c$) the system spontaneously chooses an intrinsic length scale, which results in a macroscopic long-ranged correlation visible as a spatiotemporal pattern and which is *independent* of microscopic

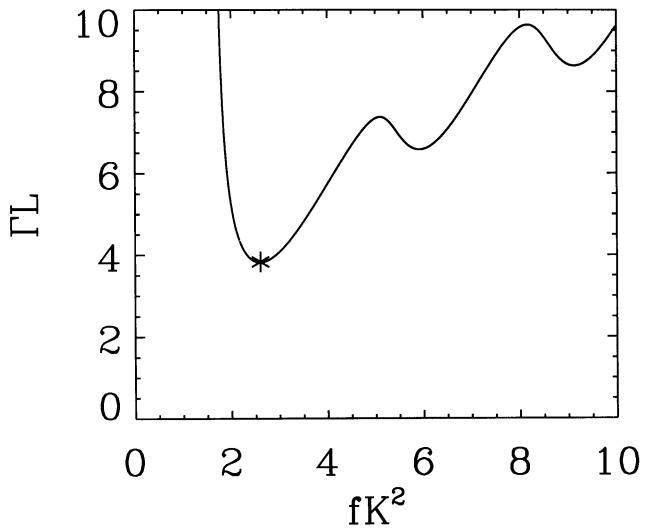

Fig. 2. Threshold curve of the coupling strength Γ as function of the transverse wave number K for a stationary instability with $D = 0$ and $R = 1$. The asterisk $(*)$ denotes the critical values K_c and Γ_c.

length scales given by the laser light or internal crystal structures, for example.

After having discussed the linear instability threshold we come back to the multiple scale analysis. Linear stability predicts the onset of a stationary modulation. Since we restrict ourselves to one transverse dimension, only modulations of the beam profile are possible (corresponding to stripe patterns in 2D). Hence one can now make the specific ansatz for a stationary stripe-like pattern:

$$\mathbf{U}^{(1)} = \mathbf{u}^{(1)}(z;\, K_c)(W\, \exp(iK_cX_0) + \text{c.c.}) \qquad (12a)$$

$$\mathbf{P}^{(1)} = \mathbf{p}^{(1)}(z;\, K_c)(W\, \exp(iK_cX_0) + \text{c.c.})\,. \qquad (12b)$$

At this stage one introduces the mode amplitude $W = W(T_1, T_2, \ldots, X_1, X_2, \ldots)$ that may still depend on the slower time and space scales.

The propagation of the transverse modulation through the bulk medium is described by a longitudinal eigenfunction $\mathbf{u}^{(1)}$. It can be calculated from the flow matrix of the linear stability problem

$$\mathbf{u}^{(1)}(z,\, K_c) = \mathcal{F}(z;\, K_c)\mathbf{u}^{(1)}(0)\,, \qquad (13)$$

where the vector of initial condition $\mathbf{u}^{(1)}(0)$ belongs to the kernel of the (inverse of the) scattering matrix $\mathcal{S}_F(K_c)$, and where $\mathbf{p}^{(1)} = \mathcal{N}_0\mathbf{u}^{(1)}$.

2.2. *Nonlinear mode interaction*

As soon as we go to higher orders in the expansion, nonlinear mode interaction occurs and spatial harmonics are generated. From the expansion in second order we have

$$\mathcal{L}^c_{z,x}\mathbf{U}^{(2)} + \mathcal{M}^c_0\mathbf{P}^{(2)} = \mathcal{L}^{(1)}\mathbf{U}^{(1)} - \mathcal{M}^{(1)}_0\mathbf{P}^{(1)} + \boldsymbol{\mathcal{M}}^c_1(\mathbf{P}^{(1)}|\mathbf{U}^{(1)})\,, \quad (14a)$$

$$\mathcal{D}_{T_0}\mathbf{P}^{(2)} - \mathcal{N}_0\mathbf{U}^{(2)} = -\mathcal{D}_{T_1}\mathbf{P}^{(1)} + \boldsymbol{\mathcal{N}}_1(\mathbf{U}^{(1)}|\mathbf{U}^{(1)})\,. \quad (14b)$$

For a stationary pattern one has $\mathcal{D}_{T_0} = 1$ and in Eq. (14b) we can again solve for the grating variable $\mathbf{P}^{(2)}$ and eliminate it from Eq. (14a) in favor of an inhomogeneous ordinary differential equation for the field variable $\mathbf{U}^{(2)}$. The inhomogeneous part generates spatial Fourier modes $K = 0$, K_c, and $2K_c$ and consequently the solution ansatz in second order is of the form

$$\begin{aligned}\mathbf{U}^{(2)}(z;\, x) = {}& \mathbf{u}^{(2)}(z;\, K=0)(|W|^2 + \text{c.c.}) \\ & + \mathbf{u}^{(2)}(z;\, K_c)(V\, \exp(iK_cx) + \text{c.c.}) \\ & + \mathbf{u}^{(2)}(z;\, 2K_c)(W^2\, \exp(2iK_cx) + \text{c.c.})\,.\end{aligned} \qquad (15)$$

Since the resonant mode is excited, a new amplitude V must be introduced. The longitudinal eigenfunctions in second order then satisfy the equation

$$\partial_z\mathbf{u}^{(2)}(z;\, K) = \mathcal{A}_c(z;\, K)\mathbf{u}^{(2)}(0;\, K) + \mathbf{s}^{(2)}(z;\, K)\,. \qquad (16)$$

The associated boundary-value problem has a solution whenever $K \neq K_c$. For the resonant mode $K = K_c$, one has to apply the solvability condition known as Fredholm alternative theorem

$$\langle \mathbf{v}(z;\, K_c)|\mathbf{s}^{(2)}(z;\, K_c)\rangle = 0 \qquad (17)$$

which involves the scalar product with the adjoint homogeneous solution $\mathbf{v}(z;\, K_c)$. In addition to the Fredholm alternative, to avoid secular terms, it must be required that $\Gamma^{(1)} = 0$ and $\partial_{T_1}W = 0$ which results in $V = -2if K_c\partial_{X_1}W$. Thus we have completely determined the longitudinal eigenfunctions in second order. Their shape and their meaning for pattern formation will be discussed in Sec. 3.1.

Saturation of the linear exponential growth is at first achieved in third order. Here nonlinear mode interaction again generates resonant and nonresonant modes. The solvability condition applied to the resonant mode determines $\Gamma^{(2)}$ and leads to the amplitude equation for a stripe-like pattern

$$\tau_0\partial_tW = (\Gamma - \Gamma_c)W + D_s\partial_x^2W - g_s|W|^2W\,. \qquad (18)$$

This is the well-known Ginzburg–Landau equation. It provides a universal description for the self-organization of patterns in 1D that is similar to a second-order phase transition [Walgraef, 1997]. The values of the relaxation rate

$$\tau_0 = -\frac{\tau}{g_0}\,\langle \mathbf{v}_{K_c}|\mathcal{M}_0^c\mathcal{N}_0|\mathbf{u}_{K_c}^{(1)}\rangle = 0.4512\tau\,, \qquad (19)$$

the diffusion constant

$$D_s = -\frac{4f^2K_c^2}{g_0}\,\langle \mathbf{v}_{K_c}|I|\mathbf{S}_{K_c}^{(2)}\rangle = 20.391f\,, \qquad (20)$$

and the nonlinear self-coupling coefficient

$$g_s = \frac{1}{g_0}\,\langle \mathbf{v}_{K_c}|\mathcal{M}_0^c\mathbf{n}_s - \mathbf{m}_s\rangle = 15.694 \qquad (21)$$

reflect the specific properties of the PR system under consideration, and they are given here for the parameters $R = 1$ and $D = 0$ that we have used in the subsequent numerical simulations (for details on g_0, D_s and $\mathbf{m}_s$, $\mathbf{n}_s$ see Appendix A).

3. Spatiotemporal Structures

The analytical treatment previously presented tells us where we can expect modulational instability. Furthermore, it approximately describes the behavior of mode amplitudes above threshold, but it cannot reveal what pattern will occur. In the following section numerical simulations of the full nonlinear model equations are presented and the pattern formation by two-wave mixing in a PR bulk medium is discussed. We also compare the numerical with the analytical results, and discuss the effect of different aspect ratios.

We used a modified beam propagation method which we extended by means of a relaxation-type integration procedure to account for the two-point boundary-value problem [Sandfuchs *et al.*, 1998] and the feedback mirror geometry. The feedback mirror with reflectivity $R = 1$ is placed at the exit face of the crystal ($D = 0$).

In optics, contrary to most of the hydrodynamic systems, e.g., the beam profiles are constrained to a finite lateral extent. A laser beam has typically a Gaussian envelope and the aspect ratio is low. A higher aspect ratio can be achieved when the beam is broadened and a plateau forms. To accomplish high aspect ratio conditions for the simulations we have chosen the incident envelope of A_1 to have the shape of a hyper-Gaussian beam of order n, whereas the envelope of A_2 obeys the mirror boundary condition

$$A_1(x,\,0,\,t) \equiv A_1\,\exp(-x^{2n})\,, \qquad (22a)$$

$$A_2(x,\,L,\,t) = -A_1(x,\,L,\,t)\,. \qquad (22b)$$

In performing the analytical treatment we assumed the homogeneous fixed-point solution to be infinitely extended, i.e. we restricted the analysis to an infinitely high aspect ratio. As a consequence one should encounter discrepancies which become predominant for lower aspect ratios, respectively less modulations occur compared to the unmodulated beam envelope [Agrawal, 1990]. Here we report the results on the cases $n = 1$ and $n = 4$. They roughly correspond to low and "high" aspect ratios, respectively. The hyper-Gaussian beam profile approximates the assumption of infinitely extended modulation from the analysis more closely. We will show that the discrepancies remain rather small in this case.

3.1. *Primary patterns in 1D*

As predicted by the linear and nonlinear analysis a primary instability in the form of a stationary modulation $|W|\,\cos(K_c x + \psi)$ develops across the uniform solution with the transverse phase shift ψ relative to the beam center. In general, ψ changes continuously because of the translational symmetry in the case of high aspect ratio systems. The homogeneous solution becomes unstable, first the hyper-Gaussian ($n = 4$) and then the ordinary Gaussian profile ($n = 1$).

In the nonlinear interaction the transverse modes $K = K_c$, $K = 0$ and $K = 2K_c$ are generated up to second order and significantly contribute to the pattern amplitude. The pattern amplitude is a superposition of mode amplitudes and eigenfunctions depending on the propagation position z where the pattern is observed. From the Ginzburg–Landau equation [Eq. (18)] the growth of the amplitude of the critical mode K_c is calculated to increase as $|W| = \sqrt{(\Gamma - \Gamma_c)/g_s}$. Equation (15) relates the growth of amplitude of the modes $K = 0$ and $K = 2K_c$ to $|W|^2 = (\Gamma - \Gamma_c)/g_s$.

The spatial modes from numerical data are localized in the near field, and have finite spot size in the optical far field. Therefore their mode amplitudes are taken as the amplitude of the envelope of the wave packet. The values of mode amplitudes are displayed in Fig. 3. The analytical curves

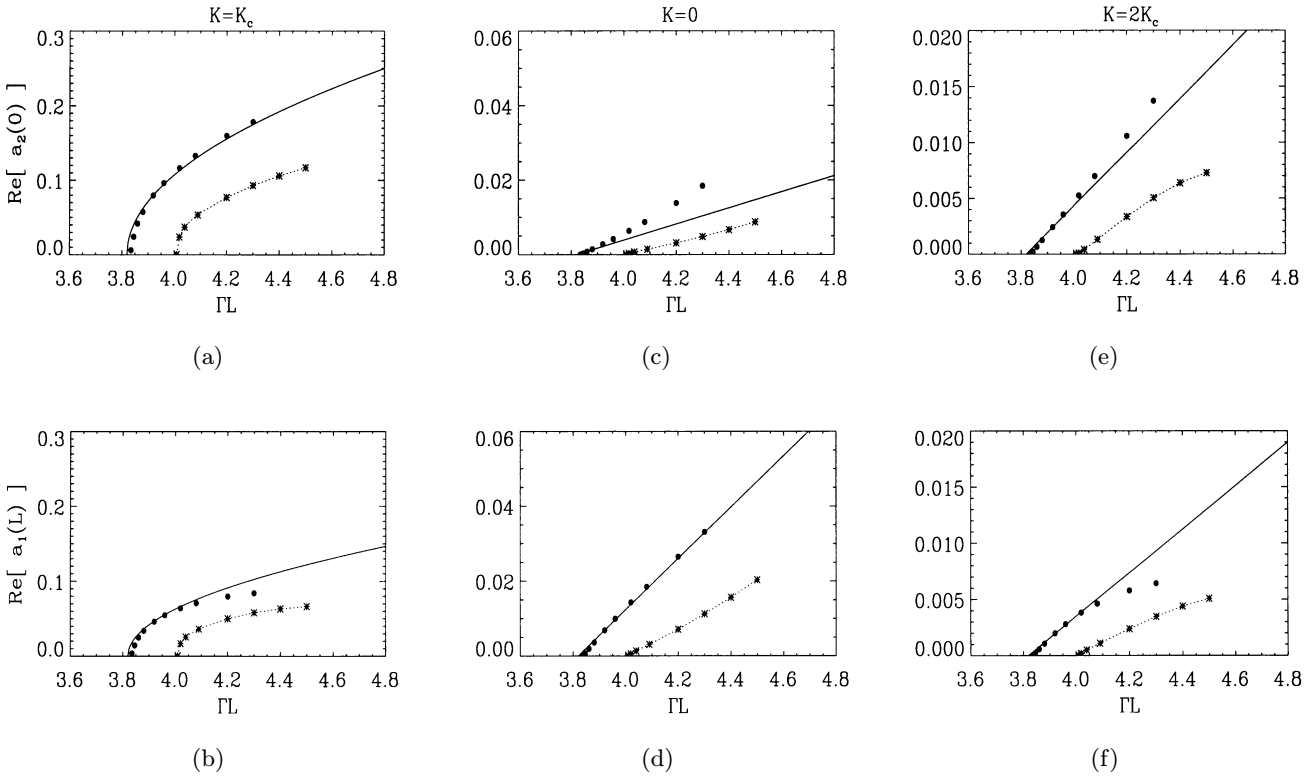

Fig. 3. The real part of the mode amplitudes $a_1(L)$ and $a_2(0)$ above the primary instability threshold as functions of coupling strength ΓL, for the three dominant modes $K = K_c$, $K = 0$ and $K = 2K_c$. The values of the eigenfunctions at these points are (a) $\eta = 1.0$, (b) $\eta = 0.586$, (c) $\eta = 0.381$, (d) $\eta = 0.308$, (e) $\eta = 0.344$, (f) $\eta = 1.089$. Analytical amplitude (solid line). Numerical results for the beam profiles: $n = 1$ ($*$), dotted line: guide to the eye; and $n = 4$ ($\bullet$).

are multiplied by the specific value η of the eigenfunction at the output faces to be equivalent to the mode amplitude obtained from numerical data. The eigenfunctions corresponding to each of the modes are shown in Fig. 4. We have displayed the real parts because they resemble the intensity modulations $\delta I_j/I_j^0 = \mathcal{R}e(a_j)+|a_j|^2$, with $|a_j|^2$ being small near threshold. The normalization of eigenfunctions is arbitrarily chosen such that $\mathcal{R}e[a_2(0)] = 1$ for $K = K_c$.

For the case of $n = 4$ the overlap between analytical and numerical data turns out to be rather good, despite the apparent difference between the "high" optical and idealized infinitely high aspect ratio. As expected, the results for the Gaussian beam profile differ considerably. This effect cannot be the consequence of the different energy contained in the beams with different n, because in the model of PR wave mixing only intensity ratios are relevant in the formation of modulational instabilities.

From the behavior of the eigenfunctions we now extract some features worthwhile mentioning. In the pattern amplitude one usually observes a strong saturation behavior as one goes further away from threshold, which may be caused by the fact that higher modes have a negative contribution (e.g. for $z = 0$ here) and thus reduce the overall pattern amplitude. Moreover, the shape of the eigenfunction for the mode $K = 0$ shows clearly an energy exchange among the pump beam and the pattern modes during the emergence of the structure. Energy is transfered into the structure as well as fed back into the pump beam.

The particular shape of the eigenfunction belonging to $K = K_c$ reveals an interesting feature of pattern formation in PR wave mixing: the pattern amplitudes at the opposite faces of the crystal show an *anti-phase* behavior. The patterns are spatially inverted with respect to each other, i.e. ψ is shifted by π dependent on whether the pattern is observed at $z = 0$ or $z = L$. It is the result of two properties: first, energy conservation of wave mixing, which requires that what is pumped into the crystal must come out, however, it cannot explain

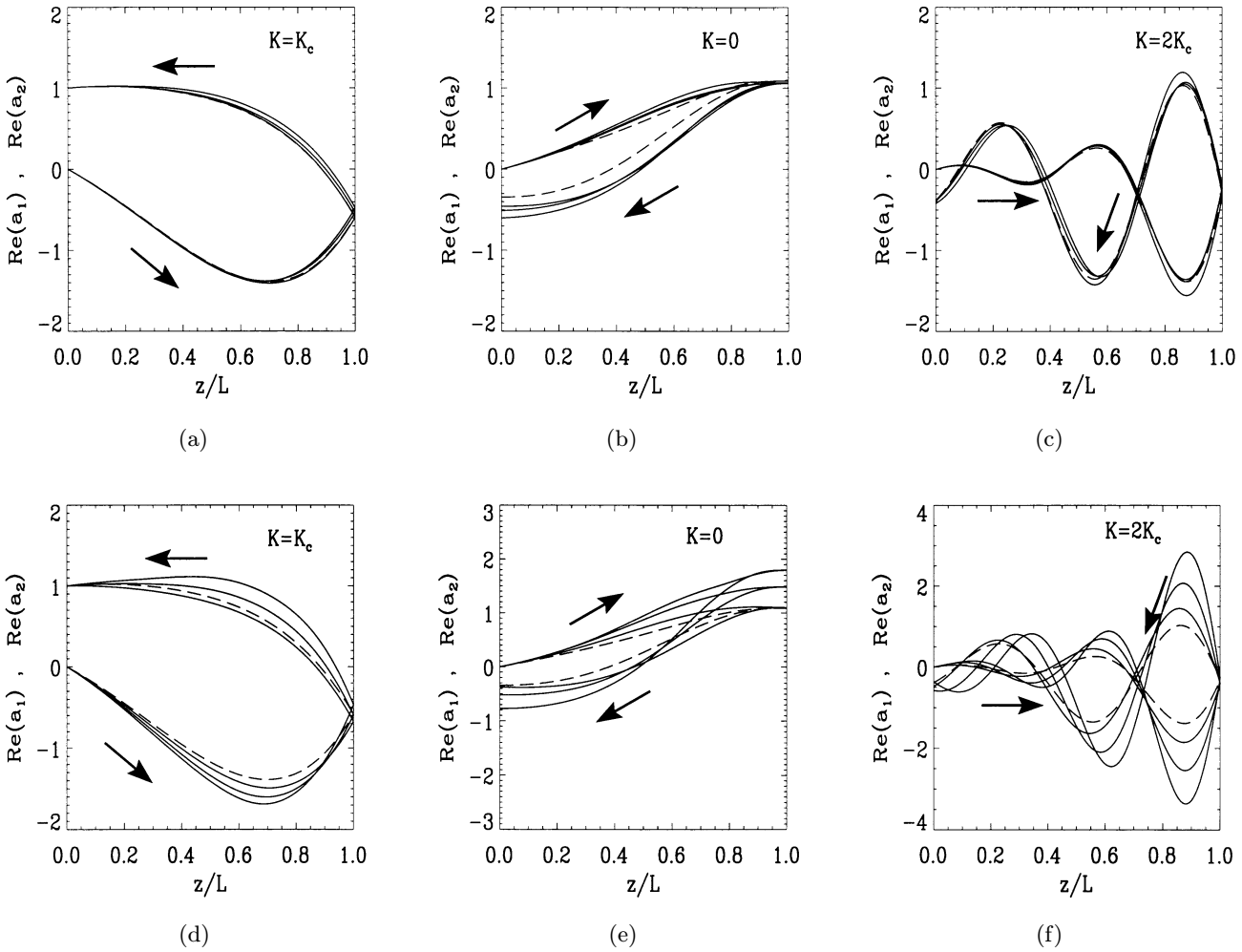

Fig. 4. Longitudinal eigenfunctions of the corresponding transverse modes (a and d) $K = K_c$, (b and e) $K = 0$ and (c and f) $K = 2K_c$ for the forward (a_1) and the backward (a_2) propagating modulations. The arrows indicate the direction of propagation. Analytical results (dashed lines), numerical simulations (solid lines) for three different values of coupling strength above threshold: $\Gamma L = 3.86$, 4.10, 4.30, (a–c) for $n = 4$; and $\Gamma L = 4.10$, 4.40, 4.80, (d–f) for $n = 1$.

the correlated spatial distribution of the two structures. But second, Eqs. (4a)–(4c) can be interpreted by four-wave mixing of the side-band beams with each other. A similar anti-phase behavior is seen in the process of phase conjugation in PR crystals [Belić *et al.*, 1995]. This feature, though, is not unique to the PR two-wave mixing and should in general be observable in other optical wave-mixing systems.

From the above discussion it becomes clear that the *absolute* value of the mode amplitude W given by the amplitude equation loses its meaning without the explicit knowledge of the longitudinal behavior in the bulk medium. The critical mode amplitude and the pattern amplitude must clearly be distinguished, and they certainly coincide only very close to threshold. However, the mode amplitudes obtained from analysis can still give rather accurate results even far away from threshold depending on how many higher modes have a significant contribution.

3.2. *Secondary bifurcations*

Further away from the primary threshold stationary patterns become unstable and secondary bifurcations occur. Upon approaching the secondary instability threshold, different things happen, depending on the aspect ratio of our system. As mentioned in the last section, in general ψ changes continuously because of the translational symmetry for very high aspect ratios. This remains true for a low aspect

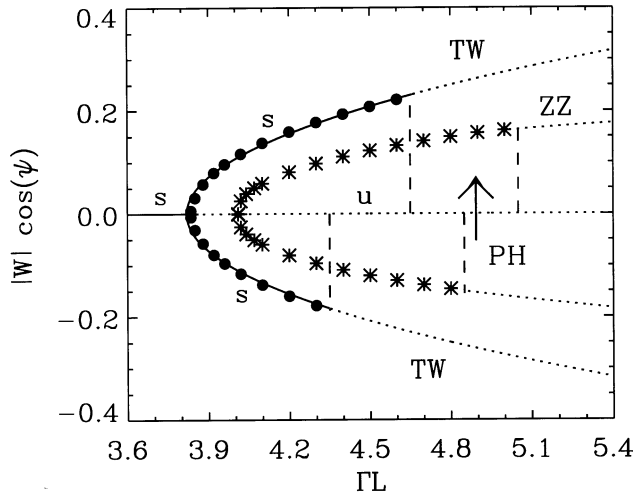

Fig. 5. Bifurcation diagram of the primary and secondary instabilities of the beam A_2 at $z = 0$, displaying the amplitude of mode K_c as a function of ΓL. Both the hyper-Gaussian ($\bullet$) and the Gaussian ($*$) cases are shown, as well as the $\psi = 0$ (upper) and $\psi = \pi$ (lower) branches, obtained from numerical simulations. The solid curves indicate analytically obtained branches, dotted lines indicate the unstable solutions. Short-dashed lines mark secondary thresholds for different cases and branches. *s* denotes stable solutions, *u* unstable ones. TW and ZZ are placed where the stable transverse wave (respectively the zig-zag) exist. PH denotes the phase-hop, and the arrow designates its direction.

ratio system close to the primary threshold. However, in numerical simulations with Gaussian beam profiles further away from threshold this symmetry is broken, owing to the finite extent of the beam envelope, and ψ assumes discrete values. Two branches of the modulation are identified, those with phase $\psi = 0$ and $\psi = \pi$, respectively. The results are presented in the bifurcation diagram (Fig. 5). Both stable branches are shown for both values of n. At the primary instability threshold the stable modulation develops and grows [cf. Fig. 3(a)], until the secondary instability threshold is reached.

The evolution of the Gaussian carrier wave ($n = 1$) differs again considerably from the hyper-Gaussian. Increasing Γ, the $\psi = \pi$ branch loses the stability first and jumps over to the $\psi = 0$ stable branch, by performing a *phase hop*. This is presented in Figs. 6(a) and 6(b). In the sequence of events, starting from the initial unstable fixed point, the system visits the $\psi = \pi$ branch (repeller). The orbit turns out to be a saddle-focus, and this branch, for the given value of Γ, is also unstable. It then performs a phase hop, to reach the stable $\psi = 0$ branch (attractor). We should note that, depending on the perturbation of the initial unstable fixed-point, the system may directly revert to the stable attractor, without visiting the repeller first. Although pattern formation at the primary threshold is bulk-controlled, this type of phase instability far above threshold is certainly triggered by boundary influences due to the low aspect ratio of a Gaussian carrier wave.

The secondary instability of the $\psi = 0$ branch of the Gaussian wave [Figs. 6(c) and 6(d)] is not a simple traveling wave. We will refer to it as a *temporal zig-zag* wave, for its appearance. Traditional zig-zag instability, however, is present in two-dimensional systems only. Apparently, time plays the role of the second dimension here. Because of this analogy we termed it temporal zig-zag wave.

Contrary, the hyper-Gaussian primary modulation loses stability to running transverse waves (TW) as in Fig. 7(a). The threshold for the $\psi = \pi$ branch is lower than the threshold for the $\psi = 0$ branch. The sources and sinks of TW are situated on the edge of the modulation-carrying wave. This is different from the counterpropagating two-wave mixing with external electric field, considered earlier [Sandfuchs *et al.*, 1999], where the source of dynamic structure sits in the middle of the wave and emits TW to the left and to the right toward the sinks at the two edges of the beam.

The wave numbers of both types of secondary waves remain indistinguishably close to K_c, and their frequencies are $\Omega\tau \approx 0.01$ where τ is typically of the order of seconds. Hence the dynamics of PR structures found is extremely slow. One refers to such spatiotemporal motion as *day-dreaming* patterns. Higher spatial modes are clearly visible in the intensity profile of the depleted beam A_1. They are a consequence of the modulus and are not dominant in the complex field amplitudes.

3.3. *Hysteresis for spatiotemporal patterns*

The amplitude of the secondary structures appears discontinuously, which is similar to a first-order phase transition, so one would expect a hysteretic behavior. In the following, the spatiotemporal behavior of the TW for $n = 4$ in the vicinity of the secondary threshold is investigated.

In experiments with PR crystals it is usually impossible to vary the coupling strength, because it is a fixed value for each crystal. The evaluation of the far field intensity from numerical data is, due to the wave packet character, much more complete

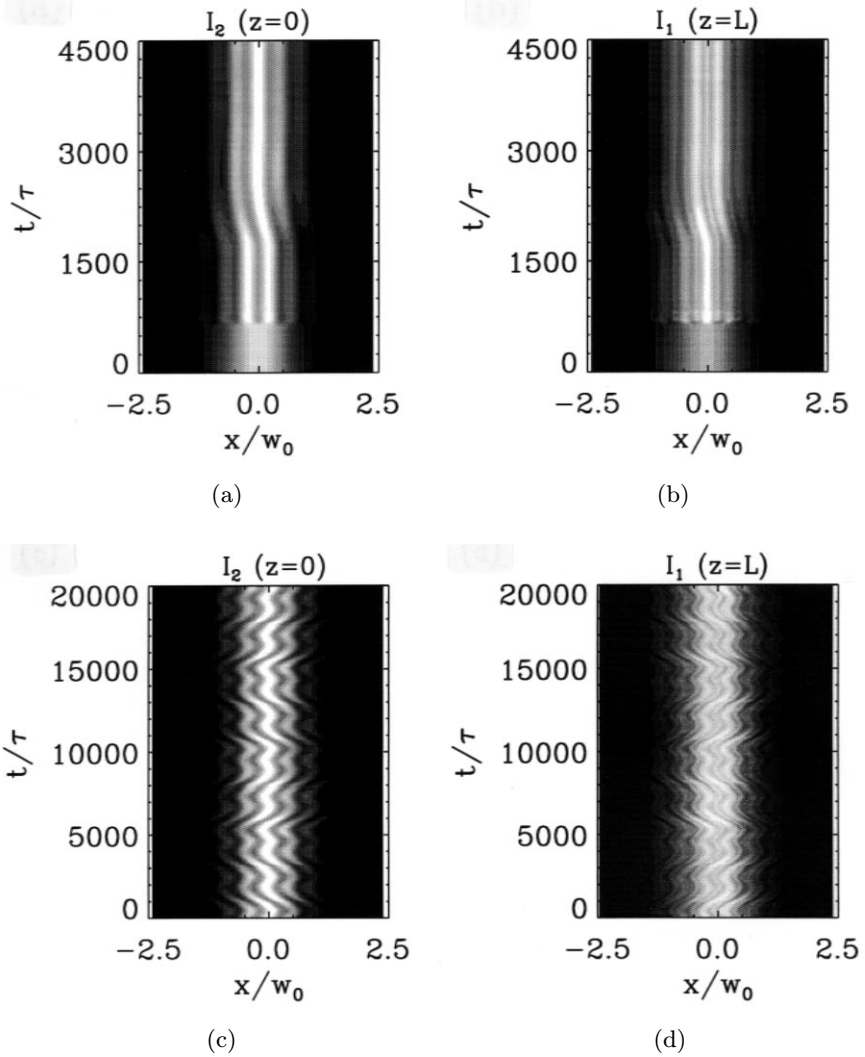

Fig. 6. Transverse intensity profiles of the beams in the near field for a Gaussian input beam $n = 1$ and $f = 0.016$. Spatiotemporal dynamics of the phase-hop instability at $\Gamma L = 4.9$ for (a) beam A_2 at $z = 0$ with $\psi = 0$ and (b) beam A_1 at $z = L$ with $\psi = \pi$. Spatiotemporal dynamics of zig-zag wave above the secondary instability threshold for $\Gamma L = 5.2$ for (c) beam A_2 at $z = 0$ with $\psi = 0$ and (d) beam A_1 at $z = L$ with $\psi = \pi$.

than obtaining the near field amplitude. And the latter is also hard to detect in experiments. In the following the mirror reflectivity R will be our bifurcation parameter. The hysteresis loop in R is equivalent to that in Γ, but the spatiotemporal behavior is visible over a broader parameter range. So instead of varying the coupling strength Γ, we vary the mirror reflectivity R and look at the side-band-to-pump intensity ratio S in the far field. The far field in optics is directly related to the Fourier modes.

Below secondary threshold reducing the mirror reflectivity from unity to zero the side-band-to-pump ratio remains almost constant until the modulation disappears. Figure 8(a) displays such curves for some values of the coupling strength. Following the upper hysteresis branch in R (at $\Gamma L = 4.7$) we surprisingly found that the TW vanishes after it has passed through two other types of TW [Figs. 7(b) and 7(c)] before. At the lower hystersis point the intensity of the TW goes continously to the stationary value of the solution, but there is a gap in the frequency that prevents the stationary pattern from reaching TW_3 when R is increased again.

The nature of secondary structures is reminiscent of a phase instability. Although, it is yet not clear if the TW is induced by a phase diffusion mechanism like in an Eckhaus instability. The TW

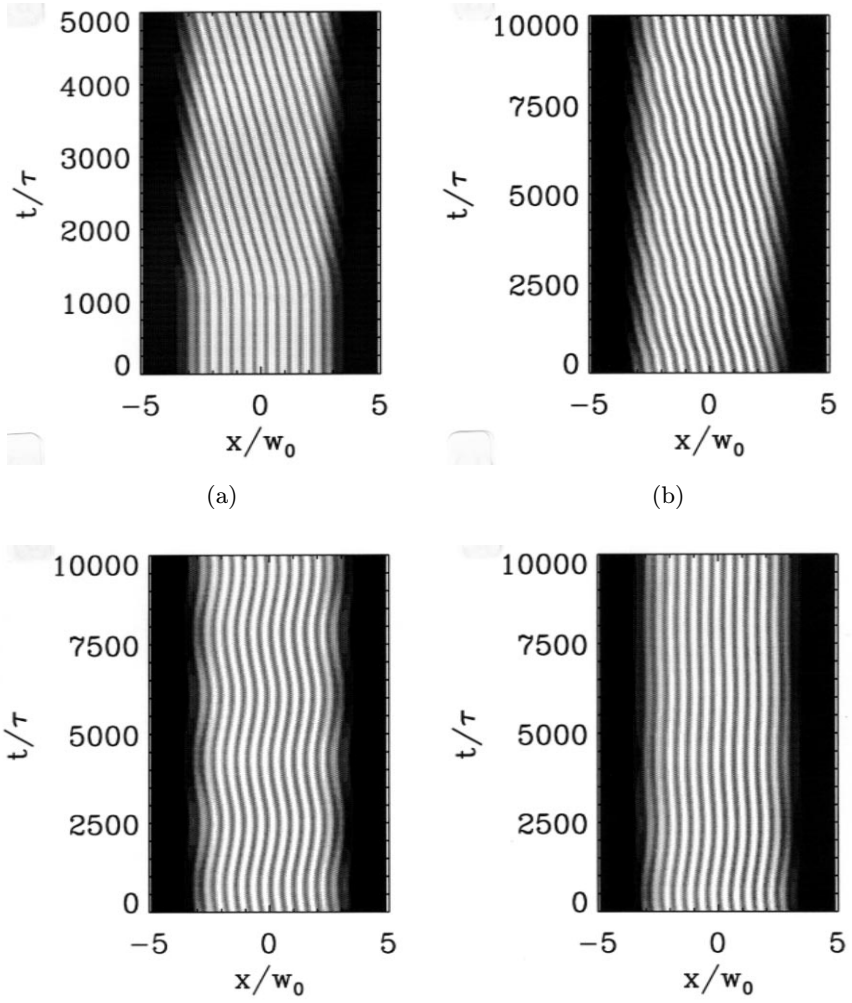

Fig. 7. Transverse intensity profiles of the beam A_2 as it leaves the crystal at $z = 0$ in the near field for a hyper-Gaussian input beam $n = 4$ and $f = 0.016$. Spatiotemporal dynamics of the transverse wave at $\Gamma L = 4.7$ for (a) developing TW_1 at $R = 0.90$, the attractors (b) TW_2 at $R = 0.50$, (c) TW_3 at $R = 0.45$, and (d) a disappearing TW at $R = 0.40$.

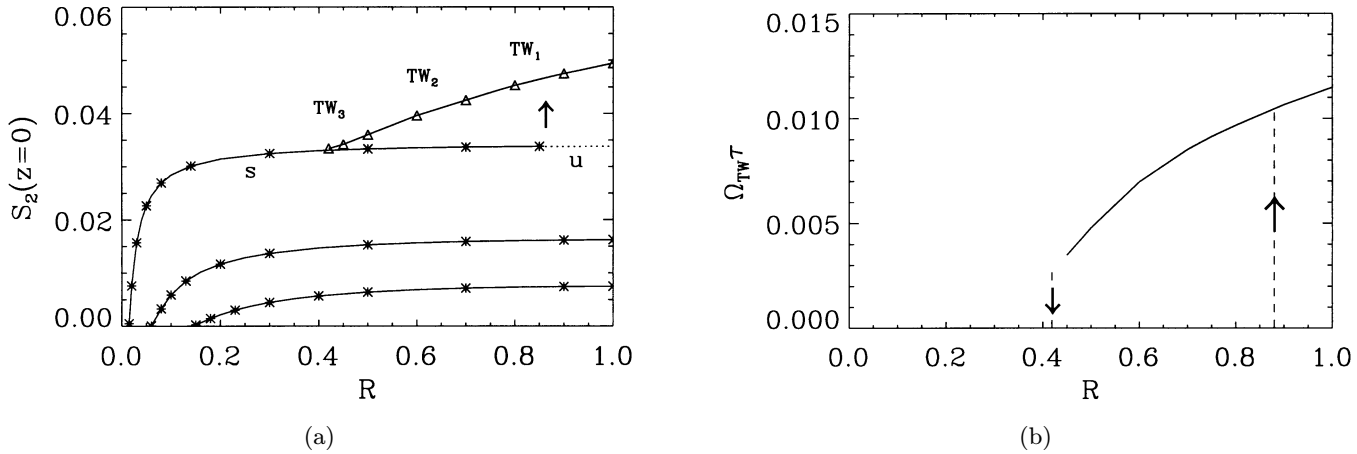

Fig. 8. (a) Side-band-to-pump ratio S of A_2 at $z = 0$ as function of the mirror relectivity R for different values of $\Gamma L = 4.0$, 4.2 and 4.7 (from bottom to top). Numerical simulations exhibiting stationary stripe pattern ($*$) and traveling waves (TW, $\triangle$) of type 1–3. Stable solutions s (solid lines) and unstable branch u (dotted line). (b) Frequency of the TW. The arrows represent the discontinous jumps at the upper and lower hysteresis points, respectively.

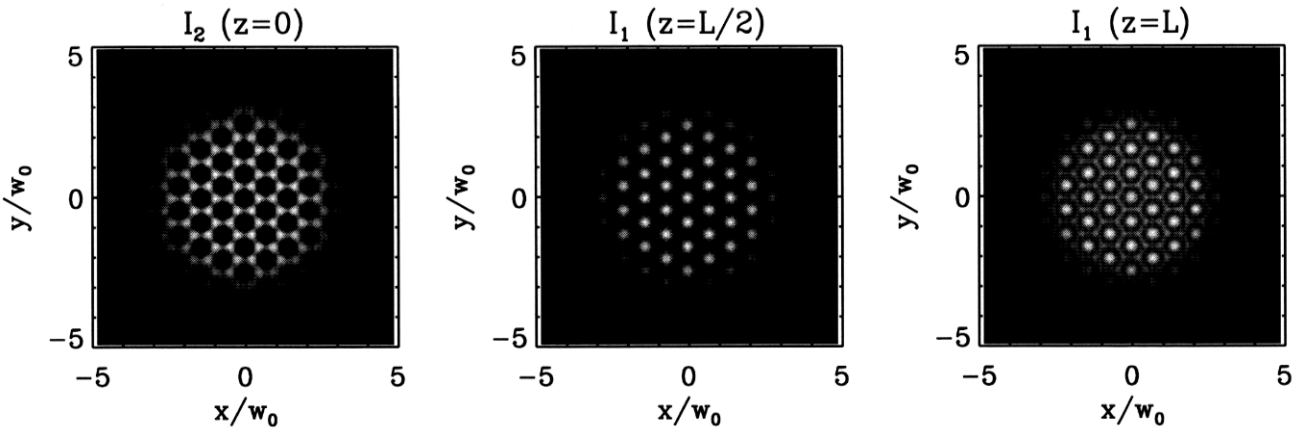

(a) (b) (c)

Fig. 9. Two-dimensional transverse beam profiles at three different positions in the crystal for $\Gamma L = 4.0$ with $n = 4$ and $f = 0.034$. (a) Inverted hexagons at $z = 0$ for beam A_2, positive hexagons at (b) $z = L/2$, and (c) $z = L$ for beam A_1 in the optical near field.

pattern possesses the same wave number K_c and a definite threshold, whereas the threshold for the Eckhaus instability depends on the wavelength ΔK with which the pattern may be disturbed (Busse balloon, [Walgraef, 1997]).

4. Primary Patterns in 2D

Here we briefly present first numerical results of primary patterns when two transverse dimensions $x \to (x, y)$ are taken into account. In the neighborhood of the primary threshold stationary hexagons are generically the only stable structures. They emerge similar to a first-order phase transition. In Fig. 9 three patterns at different positions in the crystal are shown. Again the z-dependence of the mode amplitudes forming the patterns is clearly visible. In particular the anti-phase behavior has a striking effect for the hexagonal structures: at opposite faces of the crystal one observes inverted [Fig. 9(a)] as well as positive hexagons [Fig. 9(c)] simultaneously in the respective near fields. For the positive hexagon that forms in the middle of the crystal [Fig. 9(b)] only the critical mode structure has a significant amplitude, whereas at $z = L$ mode amplitudes of the higher spatial harmonics $K = 2K_c$ and $K = \sqrt{3}K_c$, that typically arise in hexagonal planforms, dominate the intensity profile [Fig. 9(c)].

5. Conclusions

We have characterized the spatiotemporal patterns in photorefractive wave mixing with an external feedback mirror. Spatiotemporal structures arise in the counterpropagation of two optical beams and develop along the propagation through the bulk medium. We have derived a Ginzburg–Landau equation and compared the amplitude and the eigenfunctions to the results of numerical simulations in the case of low and high aspect ratios above the primary instability threshold. We found in the latter case that the agreement is rather good even further away from the primary threshold, if one clearly distinguishes the mode amplitudes from the pattern amplitude. Both 1D and 2D patterns reveal an anti-phase correlation of structures observed at the opposite faces of the crystal. Secondary structures like simple traveling and temporal zig-zag waves are observed. The traveling waves occur similar to a first-order phase transition and show a hysteretic behavior accompanied by different types of spatiotemporal structures. We did not attempt to drive the structures to spatiotemporal chaos, where we expect the relaxation-type beam-propagation method to fail in converging.

The characterization of the self-organization process of patterns presented so far for the case $D = 0$ will be extended to include real and virtual mirror distances, where the Talbot effect plays an important role [Tamburrini *et al.*, 1994], and has been the starting point for our theoretical research of pattern control by using Fourier-filter techniques.

References

Agrawal, G. P. [1990] "Transverse modulation instability of copropagating optical beams in nonlinear Kerr media," *J. Opt. Soc. Am.* **B7**, 1072–1078.

Arecchi, F. T., Boccaletti, S., Ramazza, P. L. & Residori, S. [1993] "Transition from boundary- to bulk-controlled regimes in optical pattern formation," *Phys. Rev. Lett.* **70**, 2277–2280.

Banerjee, P. P., Yu, H., Gregory, D. A., Kuhktarev, N., Caulfield, H. J. [1995] "Self-organization of scattering in photorefractive $KNbO_3$ into a reconfigurable hexagonal spot array," *Opt. Lett.* **20**, 10–12.

Belić, M. R., Leonardy, J., Timotijević, D. & Kaiser, F. [1995] "Spatiotemporal effects in double phase conjugation," *J. Opt. Soc. Am.* **B12**, 1602–1616.

Chernykh, A. I., Sturman, B. I., Aguilar, M. & Agulló-López, F. [1997] "Threshold for pattern formation in a medium with a local photorefractive response," *J. Opt. Soc. Am.* **B14**, 1754–1760.

Denz, C., Schwab, M., Sedlatschek, M., Tschudi, T. & Honda, T. [1998] "Pattern dynamics and competition in a photorefractive feedback system," *J. Opt. Soc. Am.* **B15**, 2057–2064.

Geddes, J. B., Indik, R. A., Moloney, J. V. & Firth, W. J. [1994] "Hexagons and squares in a passive nonlinear optical system," *Phys. Rev.* **A50**, 3471–3485.

Honda, T. [1993] "Hexagonal pattern formation due to counterpropagation in $KNbO_3$," *Opt. Lett.* **18**, 598–600.

Honda, T. [1995] "Flow and controlled rotation of the spontaneous optical hexagon in $KNbO_3$," *Opt. Lett.* **20**, 851–853.

Honda, T. & Banerjee, P. P. [1996] "Threshold for spontaneous pattern formation in reflection-grating-dominated photorefractive media with mirror feedback," *Opt. Lett.* **21**, 779–781.

Krolikowski, W., Belić, M. R., Cronin-Golomb, M. & Bledowski, A. [1990] "Chaos in photorefractive four-wave mixing with a single grating and a single interaction region," *J. Opt. Soc. Am.* **B7**, 1204–1209.

Kukhtarev, N. V., Markov, V. B., Odulov, S. G., Soskin, M. S. & Vinetskii, V. L. [1979] "Holographic storage in electro-optic crystals: I. Steady state + II. Beam coupling and light amplification," *Ferroelectrics* **22**, 949–964.

Leonardy, J., Kaiser, F., Belić, M. R. & Hess, O. [1996] "Running transverse waves in optical phase conjugation," *Phys. Rev.* **A53**, 4519–4527.

Lushnikov, P. M. [1998] "Hexagonal optical structures in photorefractive crystals with a feedback mirror," *J. Exp. Theor. Phys.* **86**, 614–627.

Mamaev, A. V. & Saffman, M. [1997] "Modulational instability and pattern formation in the field of non-collinear pump beams," *Opt. Lett.* **22**, 283–285.

Odoulov, S. G., Goulkov, M. Y. & Shinkarenko, O. A. [1999] "Threshold behavior in formation of optical hexagons and first order phase transition," *Phys. Rev. Lett.* **83**, 3637–3640.

Saffman, M., Zozulya, A. A. & Anderson, D. Z. [1994] "Transverse instability of energy-exchanging counter-propagating waves in photorefractive media," *J. Opt. Soc. Am.* **11**, 1409–1417.

Sandfuchs, O., Kaiser, F. & Belić, M. R. [1998] "Spatiotemporal pattern formation in counterpropagating two-wave mixing with an externally applied field," *J. Opt. Soc. Am.* **15**, 2070–2078.

Sandfuchs, O., Kaiser, F. & Belić, M. R. [1999] "Spatiotemporal dynamics in photorefractive two-wave mixing configurations: The counterpropagating geometry and the unidirectional ring oscillator," *Chaos Solit. Fract.* **10**, 709–724.

Schwab, M., Sedlatschek, M., Thüring, B., Denz, C. & Tschudi, T. [1998] "Origin and control of dynamics of hexagonal patterns in a photorefractive feedback system," *Chaos Solit. Fract.* **10**, 701–707.

Singh, N., Nadar, S. P. & Banerjee, P. P. [1997] "Time-dependent nonlinear photorefractive response to sinusoidal intensity gratings," *Opt. Commun.* **136**, 487–495.

Tamburrini, M. & Ciaramella, E. [1994] "Hexagonal beam filamentation in a liquid crystal film with single feedback mirror," *Chaos Solit. Fract.* **4**, 1355–1367.

Walgraef, D. [1997] *Spatio-Temporal Pattern Formation* (Springer, NY), Chapter 4, pp. 37–64.

Yeh, P. [1993] *Introduction to Photorefractive Nonlinear Optics* (John Wiley, NY), Chapters 1–4, pp. 1–182.

Appendix A

Here we present the details of the variables involved in the multiple scale anlysis. The basis transformation from complex vector of deviations to a real vector space reads

$$\begin{pmatrix} U_1 \\ U_2 \\ U_3 \\ U_4 \end{pmatrix} = \begin{pmatrix} 1 & 1 & -1 & -1 \\ -i & i & -i & i \\ 1 & 1 & 1 & 1 \\ -i & i & i & -i \end{pmatrix} \begin{pmatrix} a_1 \\ a_1^* \\ a_2 \\ a_2^* \end{pmatrix}, \quad \begin{pmatrix} P_1 \\ P_2 \end{pmatrix} = \begin{pmatrix} 1 & 1 \\ -i & i \end{pmatrix} \begin{pmatrix} q \\ q^* \end{pmatrix} \tag{A.1}$$

The nonlinear interaction of field amplitudes with each other and with the amplitudes of the refractive index grating leads to the following vectors

$$\boldsymbol{\mathcal{M}}_1 = \frac{\Gamma}{4} \begin{pmatrix} P_1 & P_2 & 0 & 0 \\ P_2 & -P_1 & 0 & 0 \\ 0 & 0 & -P_1 & -P_2 \\ 0 & 0 & -P_2 & P_1 \end{pmatrix} \begin{pmatrix} U_1 \\ U_2 \\ U_3 \\ U_4 \end{pmatrix} \tag{A.2}$$

and expanding the r.h.s of Eq. (4c) yields the r.h.s

of Eq. (6b)

$$\boldsymbol{\mathcal{N}}_1 = -\frac{1}{4}\begin{pmatrix} U_1^2 + U_4^2 \\ U_1U_2 + U_3U_4 \end{pmatrix} \tag{A.3}$$

$$\boldsymbol{\mathcal{N}}_2 = \frac{1}{16}\begin{pmatrix} 2U_3(U_1^2 + U_4^2) \\ 2U_1U_2U_3 - U_4(U_1^2 + U_2^2 - U_3^2 + U_4^2) \end{pmatrix} \tag{A.4}$$

They are given here for the case $R = 1$. The nonlinear self-coupling coefficient g_s depends on $\boldsymbol{\mathcal{M}}_j$ and $\boldsymbol{\mathcal{N}}_j$ over the vectors in Eq. (21)

$$\begin{aligned}\mathbf{n}_s = {} & 2\boldsymbol{\mathcal{N}}_1(\mathbf{u}^{(1)}_{K_c}|\mathbf{u}^{(2)}_{K=0}) + 2\boldsymbol{\mathcal{N}}_1(\mathbf{u}^{(2)}_{K=0}|\mathbf{u}^{(1)}_{K_c}) \\ & + \boldsymbol{\mathcal{N}}_1(\mathbf{u}^{(1)}_{K_c}|\mathbf{u}^{(2)}_{2K_c}) + \boldsymbol{\mathcal{N}}_1(\mathbf{u}^{(2)}_{2K_c}|\mathbf{u}^{(1)}_{K_c}) \\ & + 3\boldsymbol{\mathcal{N}}_2(\mathbf{u}^{(1)}_{K_c}|\mathbf{u}^{(1)}_{K_c}|\mathbf{u}^{(1)}_{K_c})\end{aligned} \tag{A.5}$$

$$\begin{aligned}\mathbf{m}_s = {} & 2\boldsymbol{\mathcal{M}}^c_1(\mathbf{p}^{(1)}_{K_c}|\mathbf{u}^{(2)}_{K=0}) + 2\boldsymbol{\mathcal{M}}^c_1(\mathbf{p}^{(2)}_{K=0}|\mathbf{u}^{(1)}_{K_c}) \\ & + \boldsymbol{\mathcal{M}}^c_1(\mathbf{p}^{(1)}_{K_c}|\mathbf{u}^{(2)}_{2K_c}) + \boldsymbol{\mathcal{M}}^c_1(\mathbf{p}^{(2)}_{2K_c}|\mathbf{u}^{(1)}_{K_c})\end{aligned} \tag{A.6}$$

where the superscript c denotes that $\boldsymbol{\mathcal{M}}_1$ has to be taken with $\Gamma = \Gamma_c$ coming from the expansion in ε, which in this case reads: $\boldsymbol{\mathcal{M}}_1 = \boldsymbol{\mathcal{M}}^c_1 + \varepsilon\boldsymbol{\mathcal{M}}^{(1)}_1 + \cdots$

The notation $(\mathbf{U}|\mathbf{U})$ and $(\mathbf{U}|\mathbf{U}|\mathbf{U})$ denotes products for different quadratic and cubic terms, respectively, as given by Eqs. (A.2)–(A.4). The scalar product in Eq. (20) defining the diffusion constant D_s involves the vector of the particular inhomogeneous solution of Eq. (16)

$$\mathbf{S}^{(2)}_{K_c}(z) = \int_0^L \mathcal{F}(z-\zeta;\, K_c)\mathbf{s}^{(2)}_{K_c}(\zeta)d\zeta \tag{A.7}$$

and the 2×2–matrix $I = ((0,\, 1),\, (-1,\, 0))$. All coefficients are divided by a common factor $g_0 = \langle \mathbf{v}_{K_c}|\tilde{\mathcal{L}} - \tilde{\mathcal{M}}_0\mathcal{N}_0|\mathbf{u}^{(1)}_{K_c}\rangle$ where $\mathcal{L} = \Gamma\tilde{\mathcal{L}}$, for example.